arXiv:1512.07257v1 [cond-mat.supr-con] 22 Dec 2015

Competing Orders in a Nearly Antiferromagnetic Metal

Yoni Schattner,[1,*] Max H. Gerlach,[2,*] Simon Trebst,[2] and Erez Berg[1]

[1]*Department of Condensed Matter Physics, The Weizmann Institute of Science, Rehovot, 76100, Israel*
[2]*Institute for Theoretical Physics, University of Cologne, 50937 Cologne, Germany*

(Dated: December 24, 2015)

We study the onset of spin-density wave order in itinerant electron systems via a two-dimensional lattice model amenable to numerically exact, sign-problem-free determinantal quantum Monte Carlo simulations. The finite-temperature phase diagram of the model reveals a dome-shaped d-wave superconducting phase near the magnetic quantum phase transition. Above the critical superconducting temperature, we observe an extended fluctuation regime, which manifests itself in the opening of a gap in the electronic density of states and an enhanced diamagnetic response. While charge density wave fluctuations are moderately enhanced in the proximity of the magnetic quantum phase transition, they remain short-ranged. The striking similarity of our results to the phenomenology of many unconventional superconductors points a way to a microscopic understanding of such strongly coupled systems in a controlled manner.

PACS numbers: 74.25.Dw, 74.40.Kb

A common feature of many strongly correlated metals, such as the cuprates, the Fe-based superconductors, heavy-fermion compounds, and organic superconductors, is the close proximity of unconventional superconductivity (SC) and spin density wave (SDW) order in their phase diagrams. This suggests that there is a common, universal mechanism at work behind both phenomena [1]. In some of these systems, additional types of competing or coexisting orders appear upon suppressing the SDW order, such as nematic, charge-density wave (CDW), or possibly also pair density wave (PDW) order. Such a complex interplay between multiple types of electronic order, with comparable onset temperature scales, is a recurring theme in strongly correlated systems [2].

These findings call for a detailed understanding of the physics of *metals on the verge of an SDW transition*. It has long been proposed that nearly–critical antiferromagnetic fluctuations can mediate unconventional superconductivity [3, 4]. Many studies have focused on the universal properties of an antiferromagnetic quantum critical point (QCP) in a metal [5–11]. In particular, it has been proposed that superconductivity is anomalously enhanced at the magnetic QCP [12–15]. The same antiferromagnetic interaction can enhance other subsidiary orders, such as CDW [14, 16, 17] or PDW [18, 19]. Near the QCP, an approximate symmetry relating the SC and density wave order may emerge [14]. The resulting multi-component order parameter would have a substantial fluctuation regime, proposed as the origin of the "pseudogap" observed in the cuprates [16, 20–22]. A deep minimum in the penetration depth of the SC at low temperature, seen in the iron-based SC $\mathrm{BaFe_2(As_{1-x}P_x)_2}$ [23], has been proposed as a generic manifestation of the underlying antiferromagnetic QCP [24, 25].

Due to the strong coupling nature of the problem of a nearly antiferromagnetic metal, obtaining analytically controlled solutions has proven difficult. In Ref. [26], a two-dimensional lattice model of a nearly-antiferromagnetic metal amenable to sign-problem-free, determinantal quantum Monte-Carlo (DQMC) simulations has been introduced. In this manuscript, we discuss the finite-temperature phase diagram obtained by large scale simulations of a closely related model. Our simulations provide numerically exact, unbiased results, which, when extrapolated to the thermodynamic limit, are highly reminiscent of the behavior of many unconventional superconductors. In the vicinity of the magnetic quantum phase transition (see Fig. 1), we find a d-wave superconducting dome with a maximum T_c of the order of $E_F/30$, where E_F is the Fermi energy. Above T_c, there is a substantial regime of strong superconducting fluctuations which is seen in a large diamagnetic response and in a reduction of the tunneling density of states. In the superconducting state we find a region of possible coexistence with SDW order [27].

In addition to SC order, we have examined CDW and PDW ordering tendencies near the magnetic quantum phase transition (QPT). While the CDW susceptibility shows a moderate enhancement in the vicinity of the QPT, there is no sign of a near-degeneracy between the SC and CDW order parameters as the QPT is approached. Finally, the low-temperature super-

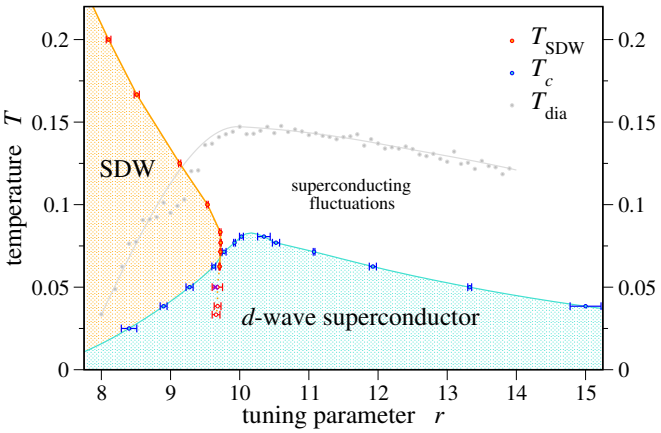

FIG. 1. (Color online) Phase diagram of model (1) showing the transition temperature T_{SDW} to magnetic spin density wave (SDW) order, the superconducting T_c, and the onset of diamagnetism at T_{dia}. The solid lines indicate a Berezinskii-Kosterlitz-Thouless transition. The SDW transition inside the SC dome, marked by a dashed line, possibly is a weakly first-order transition (see the main text).

fluid density is found to vary smoothly through the SC dome, similar to the behavior seen in the Co doped [28] and unlike the P doped [23] $BaFe_2As_2$.

Model.– Our lattice model consists of two flavors of spin–$\frac{1}{2}$ fermions, ψ_x and ψ_y, coupled to an SDW order parameter $\vec{\varphi}$. We set the magnetic ordering wavevector to $\mathbf{Q} = (\pi, \pi)$. We assume that the SDW order parameter has an *easy-plane* character, and restrict the order parameter $\vec{\varphi}$ to lie in the XY plane. Using an $O(2)$ rather than $O(3)$ order parameter (as in Ref. [26]) gives rise to a *finite-temperature* SDW phase transition of Berezinskii-Kosterlitz-Thouless (BKT) character and, on a more technical level, allows for higher numerical efficiency.

The action is $S = S_F + S_\varphi = \int_0^\beta \mathrm{d}\tau (L_F + L_\varphi)$ with

$$
\begin{aligned}
L_F = & \sum_{\substack{i,j,s \\ \alpha=x,y}} \psi^\dagger_{\alpha i s} \left[(\partial_\tau - \mu)\delta_{ij} - t_{\alpha ij} \right] \psi_{\alpha j s} \\
& + \lambda \sum_{i,s,s'} e^{i\mathbf{Q}\cdot\mathbf{r}_i} [\vec{s}\cdot\vec{\varphi}_i]_{ss'} \psi^\dagger_{xis} \psi_{yis'} + \text{h.c.}, \\
L_\varphi = & \frac{1}{2} \sum_i \frac{1}{c^2} \left(\frac{\mathrm{d}\vec{\varphi}_i}{\mathrm{d}\tau} \right)^2 + \frac{1}{2} \sum_{\langle i,j \rangle} (\vec{\varphi}_i - \vec{\varphi}_j)^2 \\
& + \sum_i \left[\frac{r}{2} \vec{\varphi}_i^2 + \frac{u}{4} (\vec{\varphi}_i^2)^2 \right]. \qquad (1)
\end{aligned}
$$

Here i, j label the sites of a square lattice, $\alpha = x, y$ are flavor indices, $s, s' = \uparrow, \downarrow$ are spin indices, and $\vec{s}$ are Pauli matrices. τ denotes imaginary time and $\beta = 1/T$ the inverse temperature. The hopping amplitudes for the ψ_x-fermions along the horizontal and vertical lattice directions are $t_{x,h} = 1$ and $t_{x,v} = 0.5$, respectively, while for the ψ_y-fermions $t_{y,h} = 0.5$ and $t_{y,v} = 1$. Note that for this choice of parameters the dispersion of the ψ_x and ψ_y fermions is quasi one-dimensional with the two bands related by a $\pi/2$ rotation. r is a tuning parameter used to tune the system to the vicinity of an SDW instability. In an experimental context, r can be thought of as doping or pressure. We set the chemical potential to $\mu = 0.5$, the quartic coupling to $u = 1$, the Yukawa coupling to $\lambda = 3$, and the bare bosonic velocity to $c = 2$.

Numerical simulations.– We study model (1) by extensive DQMC [29–32] simulations, which due to the two-flavor structure of the model do not suffer from the sign problem [26]. The simulations were performed with a single flux quantum threaded through the system, which dramatically improves the approach to the thermodynamic limit for metallic systems [33]. Specifically, we choose a magnetic flux whose direction for fermionic spin-flavor pairs $(x\uparrow, y\downarrow)$ is opposite to the one for $(x\downarrow, y\uparrow)$ pairs – a setup which avoids the reappearance of a sign problem [34, 35]. For details of this procedure and other technical aspects of the DQMC simulations and data analysis we refer to the extensive Supplemental Material. We report results up to linear extent $L = 14$ and temperatures down to $T = 0.025$.

Phase diagram.– Our main finding is the phase diagram of model (1) as shown in Fig. 1. The system displays a quasi-long-range ordered SDW phase, whose transition temperature, T_{SDW}, decreases upon increasing r. In the vicinity of the magnetic QPT where T_{SDW} collapses to zero, we find a region with quasi-long range d-wave superconducting order. The superconducting T_c traces an asymmetric dome-like shape as a function of r and reaches a maximum of $T_c^{\max} \approx 0.08$ at $r_{\mathrm{opt}} \approx 10.4$.

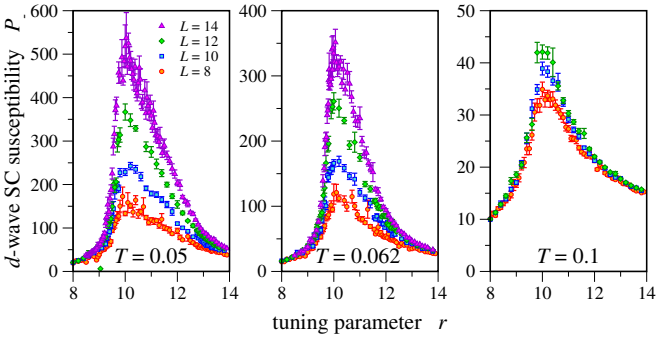

FIG. 2. (Color online) d-wave superconducting susceptibility P_- as a function of r for different system sizes and temperatures.

At sufficiently high temperatures, the antiferromagnetic transition is consistent with BKT character. In this regime the SDW susceptibility $\chi = \int d\tau \sum_i \langle \vec{\varphi}_i(\tau) \cdot \vec{\varphi}_0(0) \rangle$ for different system sizes nicely follows the expected scaling behavior $\chi \propto L^{2-\eta}$, with η changing continuously as a function of r and T, as illustrated in the Supplemental Material. We identify T_{SDW} as the point where we observe the BKT value $\eta = 1/4$. At low temperatures, $T \lesssim 0.05$ (i.e. within the SC region), the situation is less clear with the numerical data starting to systematically deviate from this scaling behavior. In fact, there are indications that the transition may become weakly first order at sufficiently low T, see the discussion in the Supplemental Material.

The SC transition is identified as the point where the superfluid density obtains the universal, BKT value $2T/\pi$ [36, 37], and is always consistent with BKT behavior. The nature of the SC phase clearly reveals itself in the d-wave pairing susceptibility $P_- = \int d\tau \sum_i \langle \Delta_-^\dagger(\mathbf{r}_i, \tau) \Delta_-(\mathbf{0}, 0) \rangle$ with $\Delta_-(\mathbf{r}_i) = \psi^\dagger_{xi\uparrow}\psi^\dagger_{xi\downarrow} - \psi^\dagger_{yi\uparrow}\psi^\dagger_{yi\downarrow}$, shown in Fig. 2. At low temperatures P_- is found to increase rapidly with system size, indicating that the SC phase has d-wave symmetry in the thermodynamic limit. The s-wave pairing susceptibility, in contrast, is found to be much smaller and system size independent [35].

A striking feature seen in the phase diagram is the "bending" of the magnetic phase boundary (indicated by T_{SDW}) near the point where it crosses the superconducting dome. An even more pronounced back bending is apparent in the magnetic susceptibility over a wide range of the tuning parameter r as shown in Fig. 3(a). Tracking the SDW susceptibility for fixed r, as shown in Fig. 3(b), one finds non-monotonic behavior with a maximum seen near T_c. Such a behavior has been predicted to arise from the competition between the two order parameters [38], and has been observed in certain unconventional superconductors, such as $Ba_{1-x}Co_xFe_2As_2$ [39].

In a finite range of temperatures above T_c, the orbital magnetic susceptibility is diamagnetic in sign (unlike the

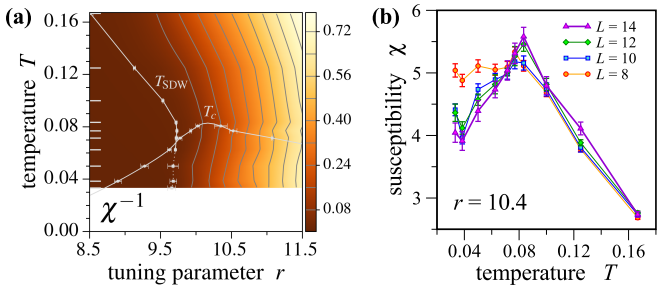

FIG. 3. (Color online) (a) Inverse magnetic susceptibility across the phase diagram with the grey lines indicating contour lines. We show data for $L = 14$ at those temperatures indicated by ticks on the left inside of the plot and interpolate linearly between them. (b) Magnetic susceptibility near the maximum of the superconducting dome ($r_{\rm opt} = 10.4$) as a function of temperature for different system sizes.

high temperature susceptibility, which is paramagnetic in our model), and its magnitude rapidly grows with decreasing temperature. We identify this behavior as a signature of substantial finite-range superconducting fluctuations. The temperature where the orbital susceptibility changes sign, denoted by $T_{\rm dia}$, is indicated by the grey dots in Fig. 1. Over much of the phase diagram, $T_{\rm dia}$ roughly follows the shape of the superconducting dome, i.e. $T_{\rm dia} \propto T_c$. Another manifestation of finite-range superconducting fluctuations is the opening of a gap in the single-particle density of states $N(\omega, T)$ above T_c. While we cannot access $N(\omega, T)$ directly without performing an analytical continuation, we can use the relation [40]

$$\begin{aligned}\tilde{N}(T) &= \frac{1}{L^2 T}\mathrm{Tr}\, G(\tau = \beta/2) \\ &= \int_{-\infty}^{\infty} \frac{d\omega}{2T\cosh(\beta\omega/2)} N(\omega, T),\end{aligned} \tag{2}$$

to extract information about the low-energy density of states, where G is the imaginary time single-particle Green's function. Note that $\tilde{N}(T \to 0) = \pi N(\omega = 0, T = 0)$. This integrated density of states $\tilde{N}(T)$ is shown in Fig. 4. In the SDW state, the behavior is consistent with a partial gapping of the Fermi surface (and corresponding suppression of the density of states), which commences slightly above the magnetic ordering temperature $T_{\rm SDW}$, see panels (a) and (b). A similar reduction of $\tilde{N}(T)$ is also found to set in above the superconducting T_c, see panels (b), (c) and (d). Extrapolating $\tilde{N}(T)$ to $T = 0$ indicates that the superconducting state is fully gapped.

CDW and PDW susceptibilities.– To explore possible CDW and PDW instabilities, we turn to examine the susceptibilities of various density-wave orders near the magnetic quantum phase transition. Specifically, we define the CDW and PDW susceptibilities

$$\begin{aligned}C_\eta(\mathbf{q}) &= \int d\tau \langle \tilde{\Delta}_\eta^\dagger(\mathbf{q}, \tau)\tilde{\Delta}_\eta(\mathbf{q}, 0)\rangle, \\ P_\eta(\mathbf{q}) &= \int d\tau \langle \Delta_\eta^\dagger(\mathbf{q}, \tau)\Delta_\eta(\mathbf{q}, 0)\rangle,\end{aligned} \tag{3}$$

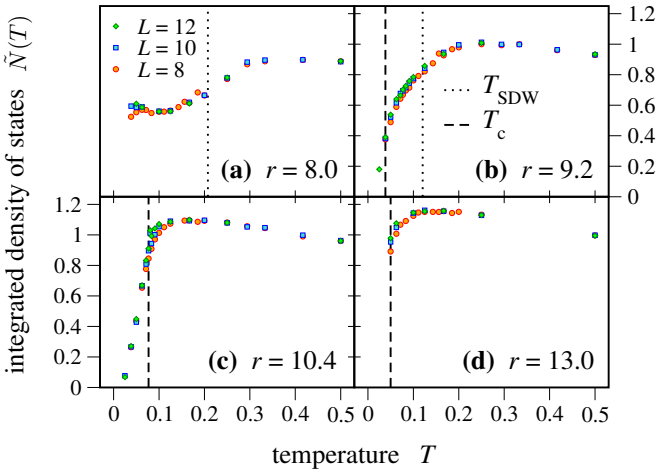

FIG. 4. (Color online) The integrated density of states $\tilde{N}(T)$, as defined in (2), versus temperature for various values of the tuning parameter r. The dashed (dotted) lines indicate the location of the SC (SDW) transition temperatures, respectively.

where $\tilde{\Delta}_\eta(\mathbf{r}_i) = \sum_{s=\uparrow,\downarrow}\left(\psi^\dagger_{xis}\psi_{xis} + \eta\psi^\dagger_{yis}\psi_{yis}\right)$ and $\Delta_\eta(\mathbf{r}_i) = \psi^\dagger_{xi\uparrow}\psi^\dagger_{xi\downarrow} + \eta\psi^\dagger_{yi\uparrow}\psi^\dagger_{yi\downarrow}$ with $\eta = \pm 1$. Note that under a $\pi/2$ rotation, associated with a rotation matrix $R_{\frac{\pi}{2}}$, we have $\Delta_\eta(\mathbf{r}) \to \eta\Delta_\eta(R_{\frac{\pi}{2}}\mathbf{r})$, i.e Δ_- has a d-wave (B_{1g}) character, and similarly for $\tilde{\Delta}_-$.

In Fig. 5 we show the momentum dependence of C_- and P_-. P_- is strongly peaked at $\mathbf{q} = 0$ and does not display much structure at other momenta, indicating that there is no noticeable tendency towards PDW order. $P_+(\mathbf{q} = 0)$ (not shown [35]) is significantly smaller in amplitude, and also shows no structure at finite momenta. C_- is maximal in the vicinity of (but away from) $\mathbf{q} = (\pi, \pi)$. $C_+(\mathbf{q})$ (not shown [35]) is qualitatively similar to $C_-(\mathbf{q})$, although its maximal value is approximately 3 times lower.

Focusing on C_-, we show its momentum dependence along the high-symmetry cut $\mathbf{q} = (\pi, q_y)$ in Fig. 6(a). The data taken from different system sizes collapses onto a single curve, suggesting that the CDW correlation length is suffi-

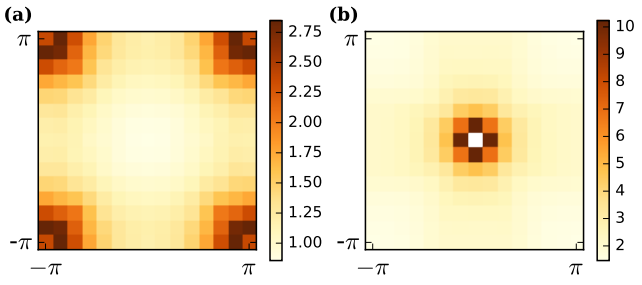

FIG. 5. (Color online) (a) d-wave CDW and (b) d-wave PDW susceptibilities, as defined in Eq. (3), across the Brillouin zone. Shown here is data for $L = 14$, $T = 0.083$, and $r = 10.4$. The data point $P_-(q = 0)$ (i.e. the uniform superconducting susceptiblity) has been excluded from the data (white square).

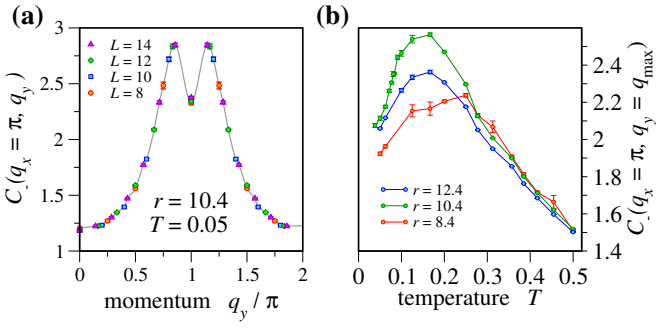

FIG. 6. (Color online) (a) The d-wave CDW susceptibility versus momentum along the high-symmetry cut $\mathbf{q} = (\pi, q_y)$ for various system sizes. The solid line is a guide to the eye. (b) Temperature dependence of the CDW susceptibility at the optimal q for multiple values of r.

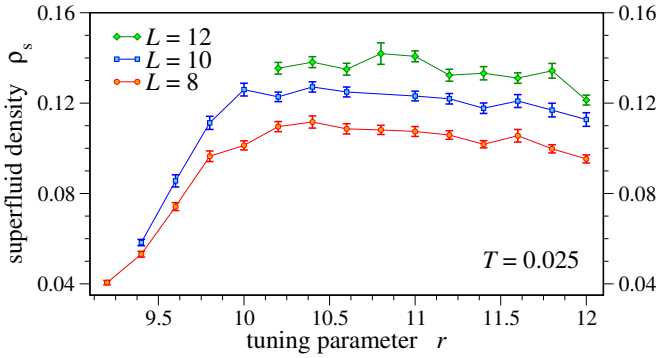

FIG. 7. (Color online) The finite-size superfluid density $\rho_s(L)$ within the superconducting phase versus r at $T = 0.025$.

ciently short such that results are representative of the thermodynamic limit. The temperature dependence of C_- at the CDW wavevector $\mathbf{q}_{\max} = (\pi, q_{\max})$ where it is maximal ($q_{\max} \approx 0.92\pi$) is shown in Fig. 6(b) for different values of r on either side of the magnetic QPT. We find that $C_-(\mathbf{q}_{\max}, T)$ is maximal at a temperature close to $\max(T_c, T_{\rm SDW})$. This can be understood as a consequence of the reduction in the density of states due to the SC or SDW order. Across the entire phase diagram, the maximal CDW susceptibility is obtained at the value of r close to the SDW QPT, where T_c is also maximal. Note, however, that near T_c the d-wave pairing susceptibility P_- is at least an order of magnitude larger than the CDW susceptibility.

Superfluid density.– Finally, we examine the low-temperature superfluid density across the phase diagram, proposed to exhibit a sharp minimum at a magnetic QCP [25]. Figure 7 shows the finite-size superfluid density $\rho_s(L)$ [35] along a cut through the superconducting dome at a fixed temperature, $T = 0.025$. Notably, we find that inside the SC dome $\rho_s(L)$ is only weakly r-dependent, with no apparent minimum at $r_{\rm opt} \approx 10.4$. This is consistent with the predictions of a field theoretical analysis [41] and with the observed behavior in $Ba_{1-x}Co_xFe_2As_2$ [39], and suggests that the sharp minimum observed in $BaFe_2(As_{1-x}P_x)_2$ may be of a different origin (see, e.g., Ref. [42]).

Discussion.– The striking similarity between the phase diagram of our model (Fig. 1) and the phase diagrams of many unconventional superconductors, such as the iron-based SC, electron-doped cuprates or organic SC, strongly suggests that much of the essential physics in these systems is indeed captured within our model, as has been long anticipated [1]. This encouraging result calls for further investigations of extensions of this basic model, designed to capture more material-specific features. For example, it would be interesting to consider a multiple component SDW order parameter (as in the pnictides), multiple bands, and additional competing order parameters. A first step in this direction has been taken recently [43].

Since models similar to the one studied here are frequently invoked to describe the phenomenology of the hole-doped cuprate superconductors, it is interesting to contrast the behavior seen in our model to that of the cuprates. Our model exhibits a gap in the single particle spectrum that precedes the phase transitions into the SC and SDW phases, as has been predicted for a nearly antiferromagnetic metal [44]. However, the onset temperature of the gap roughly follows the ordering temperature, and is never larger than about twice the corresponding transition temperature. In this sense, our results are different from the pseudogap phase of the cuprates. Our model also displays diamagnetic fluctuations with an onset temperature proportional to, and significantly above, T_c. Similar phenomena have been observed in the cuprates [45, 46].

In addition to unconventional superconductivity, our model exhibits an enhancement of CDW fluctuations with a d–wave form factor. However, the CDW susceptibility is only moderately enhanced compared to the expectation based on the non-interacting band structure. The quasi-one dimensional character of the dispersion of each fermion flavor enhances the CDW susceptibility, although at a non-zero chemical potential there is no "perfect nesting". See the Supplemental Material for a detailed comparison. It seems that the interaction mediated by spin fluctuations is not sufficient, by itself, to promote strong CDW fluctuations. This is consistent with the conclusions of Refs. [47–50] that additional, non-magnetic interactions are needed to stabilize a CDW phase.

Finally, since in our model the magnetic phase transition occurs inside a superconducting phase, our results do not have a direct bearing on the question of metallic SDW quantum criticality. In addition, we found some indications that at low temperatures, the SDW transition may become weakly first order. Nevertheless, since T_c is significantly smaller than E_F, one can still expect to see a substantial crossover regime above T_c where the physics is dominated by an underlying "avoided" QCP. Indeed, we have preliminary indications that above T_c, the dynamic SDW susceptibility exhibits Landau damping [51]. Whether this regime is characterized by a breakdown of Fermi liquid behavior, as observed in many unconventional superconductors, remains to be seen.

Acknowledgments.– The numerical simulations were performed on the CHEOPS cluster at RRZK Cologne, the JUROPA/JURECA clusters at the Forschungszentrum Jülich, and the ATLAS cluster at the Weizmann Institute. Y. S. and

E. B. were supported by the Israel Science Foundation under grant 1291/12, by the US-Israel BSF under grant 2014209, and by a Marie Curie reintegration grant. E. B. was supported by an Alon fellowship. M. G. thanks the Bonn-Cologne Graduate School of Physics and Astronomy (BCGS) for support.

Note added.– While we were preparing this manuscript, Ref. [52] appeared, where a closely related model with O(3) symmetry was studied. Our results are qualitatively similar to those of Ref. [52] where they overlap.

* These authors have contributed equally to this work.

[1] For a recent review, see: D. J. Scalapino, A common thread: The pairing interaction for unconventional superconductors, Rev. Mod. Phys. **84**, 1383 (2012).

[2] E. Fradkin, S. A. Kivelson, and J. M. Tranquada, *Colloquium* : Theory of intertwined orders in high temperature superconductors, Rev. Mod. Phys. **87**, 457 (2015).

[3] D. Scalapino, E. Loh Jr, and J. Hirsch, d-wave pairing near a spin-density-wave instability, Phys. Rev. B **34**, 8190 (1986).

[4] P. Monthoux, A. Balatsky, and D. Pines, Toward a theory of high-temperature superconductivity in the antiferromagnetically correlated cuprate oxides, Phys. Rev. Lett. **67**, 3448 (1991).

[5] J. A. Hertz, Quantum critical phenomena, Phys. Rev. B **14**, 1165 (1976).

[6] A. J. Millis, Effect of a nonzero temperature on quantum critical points in itinerant fermion systems, Phys. Rev. B **48**, 7183 (1993).

[7] A. Abanov and A. Chubukov, Spin-fermion model near the quantum critical point: one-loop renormalization group results, Phys. Rev. Lett. **84**, 5608 (2000).

[8] A. Abanov and A. Chubukov, Anomalous scaling at the quantum critical point in itinerant antiferromagnets, Phys. Rev. Lett. **93**, 255702 (2004).

[9] A. Abanov, A. Chubukov, and J. Schmalian, Quantum-critical theory of the spin-fermion model and its application to cuprates: Normal state analysis, Adv. Phys. **52**, 119 (2003).

[10] H. V. Löhneysen, A. Rosch, M. Vojta, and P. Wölfle, Fermi-liquid instabilities at magnetic quantum phase transitions, Rev. Mod. Phys. **79**, 1015 (2007).

[11] M. Metlitski and S. Sachdev, Quantum phase transitions of metals in two spatial dimensions. II. Spin density wave order, Phys. Rev. B **82**, 075128 (2010).

[12] A. Abanov, A. V. Chubukov, and A. M. Finkel'stein, Coherent vs. incoherent pairing in 2D systems near magnetic instability, Europhys. Lett. **54**, 488 (2001).

[13] A. Abanov, A. Chubukov, and M. Norman, Gap anisotropy and universal pairing scale in a spin-fluctuation model of cuprate superconductors, Phys. Rev. B **78**, 220507 (2008).

[14] M. A. Metlitski and S. Sachdev, Instabilities near the onset of spin density wave order in metals, New J. Phys. **12**, 105007 (2010).

[15] Y. Wang and A. V. Chubukov, Superconductivity at the onset of spin-density-wave order in a metal, Phys. Rev. Lett. **110**, 127001 (2013).

[16] K. B. Efetov, H. Meier, and C. Pepin, Pseudogap state near a quantum critical point, Nat. Phys. **9**, 442 (2013).

[17] Y. Wang and A. Chubukov, Charge-density-wave order with momentum $(2q, 0)$ and $(0, 2q)$ within the spin-fermion model: Continuous and discrete symmetry breaking, preemptive composite order, and relation to pseudogap in hole-doped cuprates, Phys. Rev. B **90**, 035149 (2014).

[18] Y. Wang, D. F. Agterberg, and A. Chubukov, Interplay between pair-and charge-density-wave orders in underdoped cuprates, Phys. Rev. B **91**, 115103 (2015).

[19] Y. Wang, D. F. Agterberg, and A. Chubukov, Coexistence of charge-density-wave and pair-density-wave orders in underdoped cuprates, Phys. Rev. Lett. **114**, 197001 (2015).

[20] L. E. Hayward, D. G. Hawthorn, R. G. Melko, and S. Sachdev, Angular fluctuations of a multicomponent order describe the pseudogap of yba2cu3o6+x, Science **343**, 1336 (2014).

[21] H. Meier, C. Pépin, M. Einenkel, and K. B. Efetov, Cascade of phase transitions in the vicinity of a quantum critical point, Phys. Rev. B **89**, 195115 (2014).

[22] C. Pépin, V. S. de Carvalho, T. Kloss, and X. Montiel, Pseudogap, charge order, and pairing density wave at the hot spots in cuprate superconductors, Phys. Rev. B **90**, 195207 (2014).

[23] K. Hashimoto, K. Cho, T. Shibauchi, S. Kasahara, Y. Mizukami, R. Katsumata, Y. Tsuruhara, T. Terashima, H. Ikeda, M. A. Tanatar, H. Kitano, N. Salovich, R. W. Giannetta, P. Walmsley, A. Carrington, R. Prozorov, and Y. Matsuda, A sharp peak of the zero-temperature penetration depth at optimal composition in $BaFe_2(As_{1-x}P_x)_2$, Science **336**, 1554 (2012).

[24] A. Levchenko, M. Vavilov, M. Khodas, and A. Chubukov, Enhancement of the london penetration depth in pnictides at the onset of spin-density-wave order under superconducting dome, Phys. Rev. Lett. **110**, 177003 (2013).

[25] T. Shibauchi, A. Carrington, and Y. Matsuda, A quantum critical point lying beneath the superconducting dome in iron pnictides, Annu. Rev. Condens. Matter Phys. **5**, 113 (2014).

[26] E. Berg, M. A. Metlitski, and S. Sachdev, Sign-problem-free quantum Monte Carlo of the onset of antiferromagnetism in metals, Science **338**, 1606 (2012).

[27] Our estimate for the magnetic phase boundary at low temperatures (within the superconducting phase) are less accurate than the estimate of the phase boundary at higher temperatures, since finite size effects are more pronounced in the low temperature regime (see Supplemental Material).

[28] L. Luan, T. M. Lippman, C. W. Hicks, J. A. Bert, O. M. Auslaender, J.-H. Chu, J. G. Analytis, I. R. Fisher, and K. A. Moler, Local measurement of the superfluid density in the pnictide superconductor $Ba(Fe_{1-x}Co_x)_2As_2$ across the superconducting dome, Phys. Rev. Lett. **106**, 067001 (2011).

[29] R. Blankenbecler, D. J. Scalapino, and R. L. Sugar, Monte Carlo calculations of coupled boson-fermion systems. I, Phys. Rev. D **24**, 2278 (1981).

[30] S. R. White, D. J. Scalapino, R. L. Sugar, E. Y. Loh, J. E. Gubernatis, and R. T. Scalettar, Numerical study of the two-dimensional Hubbard model, Phys. Rev. B **40**, 506 (1989).

[31] E. Loh Jr. and J. E. Gubernatis, Stable numerical simulations of models of interacting electrons in condensed-matter physics, in *Electron. Phase Transitions*, Modern Problems in Condensed Matter Sciences, Vol. 10, edited by W. Hanke and Y. Kopaev (North Holland, 1992) Chap. 4.

[32] F. Assaad and H. Evertz, World-line and determinantal quantum Monte Carlo methods for spins, phonons and electrons, in *Comput. Many-Particle Phys.*, Lect. Notes Phys., Vol. 739,

edited by H. Fehske, R. Schneider, and A. Weiße (Springer, 2008) pp. 277–356.
[33] F. F. Assaad, Depleted Kondo lattices: Quantum Monte Carlo and mean-field calculations, Phys. Rev. B **65**, 115104 (2002).
[34] Y. Schattner, S. Lederer, S. A. Kivelson, and E. Berg, Ising nematic quantum critical point in a metal: A Monte Carlo study, arXiv:1511.03282.
[35] For a detailed discussion of the numerical approach, the procedure for locating the magnetic and superconducting transitions, the calculation of the diamagnetic response, and additional data for CDW and PDW susceptibilities, see the Supplemental Material.
[36] T. Paiva, R. R. dos Santos, R. T. Scalettar, and P. J. H. Denteneer, Critical temperature for the two-dimensional attractive Hubbard model, Phys. Rev. B **69**, 184501 (2004).
[37] D. J. Scalapino, S. R. White, and S. Zhang, Insulator, metal, or superconductor: The criteria, Phys. Rev. B **47**, 7995 (1993).
[38] E. G. Moon and S. Sachdev, Competition between spin density wave order and superconductivity in the underdoped cuprates, Phys. Rev. B **80**, 035117 (2009).
[39] N. Ni, A. Thaler, J. Q. Yan, A. Kracher, E. Colombier, S. L. Bud'Ko, P. C. Canfield, and S. T. Hannahs, Temperature versus doping phase diagrams for $Ba(Fe_{1-x}TM_x)_2As_2$(TM=Ni,Cu,Cu/Co) single crystals, Phys. Rev. B **82**, 024519 (2010).
[40] N. Trivedi and M. Randeria, Deviations from Fermi-liquid behavior above T_c in 2D short coherence length superconductors, Phys. Rev. Lett. **75**, 312 (1995).
[41] D. Chowdhury, B. Swingle, E. Berg, and S. Sachdev, Singularity of the london penetration depth at quantum critical points in superconductors, Phys. Rev. Lett. **111**, 157004 (2013).
[42] D. Chowdhury, J. Orenstein, S. Sachdev, and T. Senthil, Phase transition beneath the superconducting dome in $BaFe_2(As_{1-x}P_x)_2$, Phys. Rev. B **92**, 081113(R) (2015).
[43] Z.-X. Li, F. Wang, H. Yao, and D.-H. Lee, Quantum Monte Carlo study of the T_c enhancement mechanism in FeSe on $SrTiO_3$, (2015), arXiv:1512.06179 [cond-mat.supr-con].
[44] J. Schmalian, D. Pines, and B. Stojković, Microscopic theory of weak pseudogap behavior in the underdoped cuprate superconductors: General theory and quasiparticle properties, Phys. Rev. B **60**, 667 (1999).
[45] L. Li, Y. Wang, M. Naughton, S. Ono, Y. Ando, and N. Ong, Strongly nonlinear magnetization above T_c in $Bi_2Sr_2CaCu_2O_{8+\delta}$, Europhys. Lett. **72**, 451 (2005).
[46] L. Li, Y. Wang, S. Komiya, S. Ono, Y. Ando, G. D. Gu, and N. P. Ong, Diamagnetism and cooper pairing above T_c in cuprates, Phys. Rev. B **81**, 054510 (2010).
[47] S. Sachdev and R. La Placa, Bond order in two-dimensional metals with antiferromagnetic exchange interactions, Phys. Rev. Lett. **111**, 027202 (2013).
[48] J. D. Sau and S. Sachdev, Mean-field theory of competing orders in metals with antiferromagnetic exchange interactions, Phys. Rev. B **89**, 075129 (2014).
[49] A. Allais, J. Bauer, and S. Sachdev, Density wave instabilities in a correlated two-dimensional metal, Phys. Rev. B **90**, 155114 (2014).
[50] V. Mishra and M. R. Norman, Strong coupling critique of spin fluctuation driven charge order in underdoped cuprates, Phys. Rev. B **92**, 060507 (2015).
[51] M. Gerlach, Y. Schattner, E. Berg, and S. Trebst, in preparation (2015).
[52] Z.-X. Li, F. Wang, H. Yao, and D.-H. Lee, The nature of effective interaction in cuprate superconductors: a sign-problem-free quantum Monte-Carlo study, (2015), arXiv:1512.04541 [cond-mat.supr-con].
[53] F. F. Assaad, Quantum Monte Carlo methods on lattices: The determinantal approach, in *Quantum Simulations Complex Many-Body Syst. From Theory to Algorithms*, John von Neumann Institute for Computing (NIC) Series, Vol. 10, edited by J. Grotendorst, D. Marx, and A. Muramatsu (FZ-Jülich, Jülich, Germany, 2002).
[54] R. R. dos Santos, Introduction to quantum Monte Carlo simulations for fermionic systems, Braz. J. Phys. **33**, 36 (2003).
[55] G. H. Golub and C. F. Van Loan, *Matrix Computations*, 4th ed. (The Johns Hopkins University Press, Baltimore, 2013).
[56] U. Wolff, Collective Monte Carlo updating for spin systems, Phys. Rev. Lett. **62**, 361 (1989).
[57] C. Geyer, Markov chain Monte Carlo maximum likelihood, in *Comput. Sci. Stat. Proc. 23rd Symp. Interface*, edited by E. M. Keramidas (Interface Foundation, Fairfax Station, 1991) p. 156.
[58] K. Hukushima and K. Nemoto, Exchange Monte Carlo method and application to spin glass simulations, J. Phys. Soc. Jpn. **65**, 1604 (1996).
[59] H. G. Katzgraber, S. Trebst, D. A. Huse, and M. Troyer, Feedback-optimized parallel tempering Monte Carlo, J. Stat. Mech. Theor. Exp. **2006**, P03018 (2006).
[60] S. Trebst, M. Troyer, and U. H. E. Hansmann, Optimized parallel tempering simulations of proteins. J. Chem. Phys. **124**, 174903 (2006).
[61] A. Ferrenberg and R. Swendsen, New Monte Carlo technique for studying phase transitions, Phys. Rev. Lett. **61**, 2635 (1988).
[62] A. M. Ferrenberg and R. H. Swendsen, Optimized Monte Carlo data analysis, Phys. Rev. Lett. **63**, 1195 (1989).
[63] J. D. Chodera, W. C. Swope, J. W. Pitera, C. Seok, and K. A. Dill, Use of the weighted histogram analysis method for the analysis of simulated and parallel tempering simulations, J. Chem. Theory Comput. **3**, 26 (2007).
[64] N. D. Mermin and H. Wagner, Absence of ferromagnetism or antiferromagnetism in one- or two-dimensional isotropic Heisenberg models, Phys. Rev. Lett. **17**, 1133 (1966).
[65] V. L. Berezinskii, Destruction of long-range order in one-dimensional and two-dimensional systems having a continuous symmetry group I. Classical systems, Sov. Phys. JETP **32**, 2 (1971).
[66] J. M. Kosterlitz and D. J. Thouless, Ordering, metastability and phase transitions in two-dimensional systems, J. Phys. C **6**, 1181 (1973).
[67] J. M. Kosterlitz, The critical properties of the two-dimensional XY model, J. Phys. C **7**, 1046 (1974).
[68] A. Cuccoli, V. Tognetti, and R. Vaia, Two-dimensional XXZ model on a square lattice: A Monte Carlo simulation, Phys. Rev. B **52**, 10221 (1995).
[69] G. M. Wysin, A. R. Pereira, I. A. Marques, S. A. Leonel, and P. Z. Coura, Extinction of the Berezinskii-Kosterlitz-Thouless phase transition by nonmagnetic disorder in planar symmetry spin models, Phys. Rev. B **72**, 1 (2005).
[70] W. Janke, First-order phase transitions, in *Comput. Simulations Surfaces Interfaces*, NATO Sci. Ser. II. Math. Phys. Chem., Vol. 114 (Springer Netherlands, Dordrecht, 2003) pp. 111–135.

Appendix A: Details on the Monte Carlo simulations

1. Determinantal quantum Monte Carlo setup

The action (1) defines the partition function

$$Z = \int D(\vec{\varphi}, \bar{\psi}, \psi)\, e^{-S_\varphi - S_F} = \int D\vec{\varphi}\, e^{-S_\varphi}\, \mathrm{Tr}_\psi \left[e^{-S_F}\right], \tag{A1}$$

which we now bring into a form amenable to standard determinantal quantum Monte Carlo (DQMC) methods [29, 30] as they are presented in several pedagogical texts [31, 32, 53, 54]. We also describe which measures need to be taken to attain a computational time complexity no worse than the optimal $O(\beta\mathcal{N}^3)$, where $\beta = 1/T$ is the inverse temperature and $\mathcal{N} = L^2$ the number of lattice sites.

To allow for an efficient numerical evaluation of the trace in fermionic Fock space remaining in Eq. (A1), we discretize imaginary time $\tau = \ell\Delta\tau$, $\beta = m\Delta\tau$ ($\Delta\tau = 0.1$), and after a symmetric Suzuki-Trotter decomposition we obtain

$$Z = \int D\vec{\varphi}\, e^{-\Delta\tau \sum_{\ell=1}^m L_\varphi(\ell\Delta\tau)}\, \mathrm{Tr}_\psi \left[\prod_{\ell=1}^m \hat{B}_\ell\right] + O(\Delta\tau^2). \tag{A2}$$

Here the operators $\hat{B}_\ell$ are given by

$$\hat{B}_\ell = e^{-\frac{1}{2}\Delta\tau\psi^\dagger K\psi} e^{-\Delta\tau\psi^\dagger V_\ell\psi} e^{-\frac{1}{2}\Delta\tau\psi^\dagger K\psi}, \tag{A3}$$

with non-commuting matrices K and V_ℓ and vectors of fermionic operators

$$\begin{aligned}\psi^\dagger = \left(\psi^\dagger_{\alpha i\sigma}\right) = \Big(&\psi^\dagger_{x1\uparrow}, \ldots, \psi^\dagger_{x\mathcal{N}\uparrow}, \psi^\dagger_{y1\downarrow}, \ldots, \psi^\dagger_{y\mathcal{N}\downarrow}, \\ &\psi^\dagger_{x1\downarrow}, \ldots, \psi^\dagger_{x\mathcal{N}\downarrow}, \psi^\dagger_{y1\uparrow}, \ldots, \psi^\dagger_{y\mathcal{N}\uparrow}, \Big).\end{aligned} \tag{A4}$$

Explicitly, K and V_ℓ are given by

$$\begin{aligned}K_{ij,\alpha\alpha',ss'} &= \delta_{ss'}\delta_{\alpha\alpha'}(-t_{\alpha,s,ij} - \mu\delta_{ij}), \\ V_{\ell;ij,\alpha\alpha',ss'} &= \lambda[\sigma_1]_{\alpha\alpha'}\delta_{ij}[\vec{s}\cdot\vec{\varphi}_i(\ell)]_{ss'}.\end{aligned} \tag{A5}$$

In this equation the Pauli matrix σ_1 acts on flavor indices, while the Pauli matrices $\vec{s}$ act on spin indices. We allow the hopping constants t to depend on spin in order to implement a generalized magnetic field as described in Sec. A 2 below. In this $O(2)$-symmetric model we have $\vec{\varphi} = (\varphi^1, \varphi^2)$. Carrying out the trace in Eq. (A2) yields

$$\mathrm{Tr}_\psi \left[\prod_{\ell=1}^m \hat{B}_\ell\right] = \det\left[\mathbb{1} + \prod_{\ell=1}^m B_\ell\right] = \det G_\varphi^{-1} \tag{A6}$$

with $B_\ell = e^{-\frac{1}{2}\Delta\tau K} e^{-\Delta\tau V_\ell} e^{-\frac{1}{2}\Delta\tau K}$ [32]. The matrix G_φ is the equal-time Green's function evaluated for one bosonic spin configuration $\{\vec{\varphi}_i(\ell\Delta\tau)\}$. After partitioning the matrix exponentials into $\mathcal{N}\times\mathcal{N}$-sized blocks, they read

$$\begin{aligned}e^{-\frac{\Delta\tau}{2}K} &= \mathrm{diag}\left(e^{-\frac{\Delta\tau}{2}K^\uparrow_x}, e^{-\frac{\Delta\tau}{2}K^\downarrow_y}, e^{-\frac{\Delta\tau}{2}K^\downarrow_x}, e^{-\frac{\Delta\tau}{2}K^\uparrow_y}\right), \\ e^{-\Delta\tau V(\ell)} &= \begin{pmatrix} C & S & & \\ S^* & C & & \\ & & C & S^* \\ & & S & C \end{pmatrix} = \begin{pmatrix} \widetilde{V}(\ell) & \\ & \widetilde{V}^*(\ell) \end{pmatrix}\end{aligned} \tag{A7}$$

with submatrices

$$\begin{aligned}C_{ij} &= \delta_{ij}\cosh\left(\Delta\tau|\vec{\varphi}_j(\ell)|\right), \\ S_{ij} &= \delta_{ij}\left[i\varphi^2_j(\ell) - \varphi^1_j(\ell)\right]\sinh\left(\Delta\tau|\vec{\varphi}_j(\ell)|\right)/|\vec{\varphi}_j(\ell)|.\end{aligned} \tag{A8}$$

Under the condition

$$K^\uparrow_x = K^{\downarrow,*}_x \qquad \text{and} \qquad K^\downarrow_y = K^{\uparrow,*}_y \tag{A9}$$

the Green's function decomposes into two blocks of size $2\mathcal{N}\times 2\mathcal{N}$:

$$G_\varphi = \begin{pmatrix} \widetilde{G}_\varphi & \\ & \widetilde{G}^*_\varphi \end{pmatrix}. \tag{A10}$$

Hence we can write the partition function as

$$Z = \int D\vec{\varphi}\, e^{-\Delta\tau\sum_{\ell=1}^m L_\varphi(\ell\Delta\tau)} \left|\det \widetilde{G}^{-1}_\varphi\right|^2 + O(\Delta\tau^2), \tag{A11}$$

which now is in a form that can be evaluated by Monte Carlo sampling over space-time configurations $\{\vec{\varphi}_i(\ell)\}$. Note that the probability measure under the field integral is positive definite, which allows for efficient sign-problem-free Monte Carlo simulations. The $O(2)$-symmetry allows us to restrict all fermionic evaluations to the $(x\uparrow, y\downarrow)$-sector, which speeds up the most expensive computations by a factor of 8 in comparison to the $O(3)$-model. From the matrix G_φ we can compute arbitrary fermionic equal-time observables via Wick's theorem and also access imaginary-time-displaced correlation functions after the application of matrices B_ℓ and B_ℓ^{-1}.

Generally, in the DQMC algorithm we frequently need to compute products of the matrices B_ℓ. While the exponentials of V_ℓ are sparse matrices and consequently their multiplication has a computational cost of $O(\mathcal{N}^2)$ only, even for electron hopping restricted to nearest-neighbor sites, the exponentials of the kinetic matrices K^s_α are densely filled, which raises the cost of a single multiplication to $O(\mathcal{N}^3)$. We avoid paying this cost by performing a "checkerboard" decomposition [53], where we divide the whole set of lattice bonds into two groups, so that $K^{s\,(1,2)}_\alpha$ are sums of commuting four-site hopping matrices and $K^s_\alpha = K^{s\,(1)}_\alpha + K^{s\,(2)}_\alpha$. Applying this decomposition for all α and s, we find

$$\begin{aligned}B_\ell &= e^{-\Delta\tau K/2} e^{-\Delta\tau V_\ell} e^{-\Delta\tau K/2} \\ &\approx e^{-\Delta\tau K^{(1)}/2} e^{-\Delta\tau K^{(2)}/2} e^{-\Delta\tau V_\ell} e^{-\Delta\tau K^{(2)}/2} e^{-\Delta\tau K^{(1)}/2}\end{aligned} \tag{A12}$$

and do not introduce any error of higher order than that already present from the Suzuki-Trotter decomposition, yet save one power of $\mathcal{N}$ in computational effort.

2. Controlling finite-size effects

Simulations of metallic systems at low temperatures are particularly susceptible to strong finite-size effects. Since our numerical methods limit us to the study of finite lattices, reducing the severity of these effects is very important. A dramatic reduction of finite-size effects can be obtained in the presence of a perpendicular magnetic field [33]. In our simulations we thread a single magnetic flux quantum Φ_0 through the system, making sure not to break condition (A9) in order not to re-introduce a sign problem. Specifically, we add Peierls phase factors to the hopping terms of the kinetic operator:

$$t_{\alpha,s,ij}\psi^\dagger_{x,i,s}\psi_{x,j,s} \to e^{iA^{\alpha s}_{ij}} t_{\alpha,s,ij}\psi^\dagger_{\alpha,i,s}\psi_{\alpha,j,s} \quad \text{with}$$
$$A^{\alpha s}_{ij} = \frac{2\pi}{\Phi_0}\int_{\mathbf{r}_i}^{\mathbf{r}_j} \mathrm{d}\mathbf{x}\cdot\mathbf{A}^{\alpha s} \tag{A13}$$

and choose the Landau gauge $\mathbf{A}^{\alpha s}(\mathbf{x}) = -B^{\alpha s}x_2\hat{\mathbf{e}}_1$. The sign of the magnetic field depends on flavor and spin indices α, s and its magnitude is the smallest possible on the periodic $L\times L$ lattice:

$$B^{x\uparrow} = B^{y\downarrow} = -B^{x\downarrow} = -B^{y\uparrow} = \frac{\Phi_0}{L^2}. \tag{A14}$$

Note that as $L\to\infty$ the original hopping constants are restored. To maintain translational invariance in presence of the magnetic flux we impose special boundary conditions in the $\hat{\mathbf{e}}_2$-direction

$$\psi_{\alpha,\mathbf{r}+L\hat{\mathbf{e}}_2,s} = \psi_{\alpha,\mathbf{r},s}\exp\left(\frac{2\pi i}{\Phi_0}B^{\alpha s}L\,r_1\right), \tag{A15}$$

while we retain regular periodic boundary conditions in $\hat{\mathbf{e}}_1$-direction. Explicitly, for nearest-neighbor hopping, the phases read

$$A_{ij} = \begin{cases} -\frac{2\pi}{\Phi_0}B^{\alpha s}\,i_2 & \text{if } i_1 = 0,\dots,L-2 \text{ and } j_1 = i_1+1 \\ & \text{or } i_1 = L-1 \text{ and } j_1 = 0, \\ +\frac{2\pi}{\Phi_0}B^{\alpha s}\,i_2 & \text{if } i_1 = 1,\dots,L-1 \text{ and } j_1 = i_1-1 \\ & \text{or } i_1 = 0 \text{ and } j_1 = L-1, \\ +\frac{2\pi}{\Phi_0}B^{\alpha s}L\,i_1 & \text{if } i_2 = L-1 \text{ and } j_2 = 0, \\ -\frac{2\pi}{\Phi_0}B^{\alpha s}L\,i_1 & \text{if } i_2 = 0 \text{ and } j_2 = L-1, \\ 0 & \text{otherwise,} \end{cases} \tag{A16}$$

where the lattice site vectors are $\mathbf{r}_i = (i_1, i_2)$ and $\mathbf{r}_j = (j_1, j_2)$, which we index from 0 to $L-1$ in each direction.

3. Local and global updates

The foundation of our Monte Carlo simulations of the lattice field theory (A11) is the Metropolis algorithm, where a proposed change of a bosonic field configuration $\{\vec{\varphi}\}\to\{\vec{\varphi}\,'\}$ is accepted with probability

$$p = \min\left\{1, e^{-(S'_\varphi - S_\varphi)}\left|\frac{\det\widetilde{G}_\varphi}{\det\widetilde{G}'_\varphi}\right|^2\right\}. \tag{A17}$$

The most important type of proposed changes is the local update. For one sweep of local updates we attempt to change the orientations and lengths of individual bosonic spins $\vec{\varphi}_i(\tau = \ell\Delta\tau)$ chosen sequentially from the space-time lattice. During an initial equilibration phase we generally tune the size of the box from which the new spin is chosen such that about 50% of all local updates are accepted. For local updates the determinant ratio in (A17) is given by

$$\det\widetilde{G}_\varphi/\det\widetilde{G}'_\varphi = \det[\mathbb{1} + \Delta(\mathbb{1} - \widetilde{G}_\varphi(\ell))], \tag{A18}$$

where $\widetilde{G}_\varphi(\ell) \equiv [\mathbb{1} + \widetilde{B}_\ell\cdots\widetilde{B}_1\widetilde{B}_m\cdots\widetilde{B}_{\ell+1}]^{-1}$ and $\Delta \equiv \widetilde{B}'_\ell\widetilde{B}_\ell^{-1} - \mathbb{1} = e^{-\Delta\tau\widetilde{V}'_\ell}e^{\Delta\tau\widetilde{V}_\ell} - \mathbb{1}$. We find that an expansion by minors reduces the determinant in Eq. (A18) to that of a 2×2-matrix $M = \mathbb{1}_2 + (\mathbb{1}_2 - \widetilde{G}^i)\cdot\Delta^i$, where $\Delta^i = \Delta[i::\mathcal{N}, i::\mathcal{N}]$, $\widetilde{G}^i = \widetilde{G}_\varphi(\ell)[i::\mathcal{N}, i::\mathcal{N}]$, and the slice index notation corresponds to the four sole non-zero entries of Δ. Thus the acceptance probability can be computed in constant time.

After an accepted local update the Green's function matrix must be updated:

$$\widetilde{G}'_\varphi(\ell) = \widetilde{G}_\varphi(\ell)[\mathbb{1} + \Delta(\mathbb{1} - \widetilde{G}_\varphi(\ell))]^{-1}, \tag{A19}$$

where we can again exploit the sparseness of Δ and replace the inversion of the $2\mathcal{N}\times 2\mathcal{N}$-matrix by that of a 2×2-matrix if we make use of the Sherman-Morrison-Woodbury formula [55]. In this manner we find

$$\widetilde{G}'_\varphi(\ell) = \widetilde{G}_\varphi(\ell) + (\widetilde{G}_\varphi(\ell)[:, i::\mathcal{N}]\cdot\Delta^i) \cdot\left(M^{-1}\cdot\{(G_\varphi(\ell) - \mathbb{1})[i::\mathcal{N}, :]\}\right), \tag{A20}$$

which, if the matrix products are carried out in the order indicated by the parentheses, can be evaluated with only $O(\mathcal{N}^2)$ operations. In consequence, one total sweep of local updates has a time complexity of $O(\beta\mathcal{N}^3)$.

Using only these local updates, Monte Carlo simulations of this model require relatively long thermalization periods without measurements to equilibrate the system and then generally show long statistical autocorrelation times, which are amplified near the magnetic phase transition by the effect of critical slowing down. To counteract these effects we adopt two tools: a simple global update and a replica exchange mechanism.

The global move consists of adding a constant random displacement $\vec{\delta}$ to all bosonic spins: $\vec{\varphi}_i(\tau)\to\vec{\varphi}_i(\tau)+\vec{\delta}$. To evaluate the acceptance probability (A17) we compute $\widetilde{G}'_\varphi$ and its determinant from scratch, which takes $O(\beta\mathcal{N}^3)$ operations. At times we found it also helpful to combine this move with the Wolff single cluster algorithm [56]. Here we ignore the fermionic part of the action while we construct and flip a cluster of spins, then we add the global displacement, and finally we decide on accepting the joint move according to Eq. (A17).

4. Replica exchange

For the replica exchange or parallel tempering scheme [57, 58] we consider an extended ensemble composed of multiple grand-canonical ensembles with the parameter r in S_φ taking on different values $r_1 < r_2 < \ldots < r_K$ such that the partition function is given by a product $\mathcal{Z} = \prod_{\kappa=1}^{K} Z(r_\kappa)$,

$$\mathcal{Z} = \int D(\vec{\varphi}_1, \ldots, \vec{\varphi}_K) \prod_{\kappa=1}^{K} e^{-S_\varphi(r_\kappa, \{\vec{\varphi}_\kappa\})} \left| \det \widetilde{G}^{-1}_{\varphi_\kappa} \right|^2, \tag{A21}$$

where $\widetilde{G}_{\varphi_\kappa}$ does not depend on r_κ. In the Monte Carlo simulation we then have in parallel a separate replica of the system for every r_κ, each being represented by a different system configuration. The control parameter r is treated as a dynamical variable by allowing exchanges of the configurations between replicas of different parameter values. In this way shorter autocorrelation times at high r can be utilized to accelerate the simulation across the phase transition and in the low-r region. To achieve this we need to construct a Monte Carlo move between replicas, which will supplement the single-replica local and global updates that are still carried out as in regular canonical simulations. In such an update we propose the exchange of configurations $\{\vec{\varphi}\}$ and $\{\vec{\varphi}\,'\}$ between the κ-th and η-th replicas. To ensure detailed balance we require

$$\begin{aligned} &P(\ldots, \vec{\varphi}, r_\kappa, \ldots, \vec{\varphi}\,', r_\eta, \ldots) W(\vec{\varphi}, r_\kappa | \vec{\varphi}\,', r_\eta) \\ &= P(\ldots, \vec{\varphi}\,', r_\kappa, \ldots, \vec{\varphi}, r_\eta, \ldots) W(\vec{\varphi}\,', r_\kappa | \vec{\varphi}, r_\eta), \end{aligned} \tag{A22}$$

where $P(\vec{\varphi}_1, r_1, \ldots, \vec{\varphi}_K, r_K)$ is the equilibrium probability of a set of system configurations $\{\vec{\varphi}_\kappa\}$ associated to parameters r_κ in the extended ensemble and W is the transition probability for a replica configuration exchange. The ratio of these transition probabilities is

$$\frac{W(\vec{\varphi}, r_\kappa | \vec{\varphi}\,', r_\eta)}{W(\vec{\varphi}\,', r_\kappa | \vec{\varphi}, r_\eta)} = \frac{e^{-S_\varphi(r_\kappa, \{\vec{\varphi}\,'\}) - S_\varphi(r_\eta, \{\vec{\varphi}\})}}{e^{-S_\varphi(r_\kappa, \{\vec{\varphi}\}) - S_\varphi(r_\eta, \{\vec{\varphi}\,'\})}} = e^{-\Delta}, \tag{A23}$$

where $\Delta = (r_\kappa - r_\eta) \cdot \frac{1}{2} \int_0^\beta d\tau \sum_i \left[\vec{\varphi}\,'_i(\tau)^2 - \vec{\varphi}_i(\tau)^2 \right]$ and we note that the fermion determinants have canceled. To fulfill the relation (A23) we choose exchange probabilities according to the Metropolis criterion

$$W(\vec{\varphi}, r_\kappa | \vec{\varphi}\,', r_\eta) = \min\left\{1, e^{-\Delta}\right\}. \tag{A24}$$

In our simulations we only propose exchanges between adjacent pairs of control parameter values. At high temperatures we achieve good diffusion with a simple linear spacing of the values of r. At lower temperatures, however, the magnetic phase transition constitutes a more significant barrier to the random walk in r-space. Here we have used a feedback-optimized distribution of r-values [59, 60], which effectively clusters the r_κ around $r_{\mathrm{SDW}}(T)$, easing diffusion and significantly lowering autocorrelation times. Since the exchange algorithm following Eq. (A23) does not require the recomputation of Green's functions or the evaluation of their determinants, it poses very little overhead in computation or communication. This allows us to perform a replica-exchange sweep after every single sweep of canonical updates, which has been very beneficial for obtaining sufficient statistics to resolve the magnetic phase diagram.

5. Time series reweighting

The structure of the action (1), where the r-dependence is fully contained in the bosonic part S_φ, allows to easily relate the canonical probability distribution of a configuration $\{\vec{\varphi}\}$ at a tuning parameter value r, $p_r(\vec{\varphi})$, to the distribution at another value r': $p_{r'}(\vec{\varphi}) \propto e^{-(r'-r)E(\vec{\varphi})} p_r(\vec{\varphi})$, where $E(\vec{\varphi}) = \frac{1}{2} \int_0^\beta \mathrm{d}\tau \sum_i \vec{\varphi}_i(\tau)^2$. From this relation one finds an expression for the expectation value of an observable $\mathcal{O}$ at r' in terms of expectation values at r, which in turn can be estimated by time series averages from a Monte Carlo simulation carried out at r:

$$\langle \mathcal{O} \rangle_{r'} = \frac{\langle \mathcal{O} e^{-(r'-r)E} \rangle_r}{\langle e^{-(r'-r)E} \rangle_r} \approx \frac{\sum_n \mathcal{O}_n e^{-(r'-r)E_n}}{\sum_n e^{-(r'-r)E_n}}, \tag{A25}$$

where n goes over the series of measured samples and $\mathcal{O}_n$ and E_n are computed from the same system configuration. This reweighting procedure [61] is effective over quite a wide range around r.

From our replica exchange simulations we have Monte Carlo data for multiple close values of r. We can use the combined information from these time series for r_κ, $\kappa = 1, \ldots, K$, to obtain improved observable estimates at $r_1 \leq r \leq r_K$ by multiple histogram reweighting [62, 63]. To do so we write the expectation value as

$$\begin{aligned} \langle \mathcal{O} \rangle_r &= \frac{\int \mathrm{d}E \Omega(E) e^{-rE} \mathcal{O}(E)}{\int \mathrm{d}E \Omega(E) e^{-rE}} \quad \text{with} \\ \mathcal{O}(E) &= \frac{\int D\vec{\varphi} \delta(E[\vec{\varphi}] - E) \mathcal{O}[\vec{\varphi}]}{\int D\vec{\varphi} \delta(E[\vec{\varphi}] - E)}, \end{aligned} \tag{A26}$$

where all non-r-dependent parts of the action are contained in the density of states $\Omega(E)$. We discretize E into levels E_α spaced ΔE apart and search the optimal estimator for $\Omega(E_\alpha)$, which reads

$$\hat{\Omega}_\alpha = \frac{\sum_\kappa H_{\alpha\kappa} [g_{\alpha\kappa} (1 - \Delta E \hat{\Omega}_\alpha e^{-r_\kappa E_\alpha + f_\kappa})]^{-1}}{\sum_\kappa M_\kappa \Delta E e^{-r_\kappa E_\alpha + f_\kappa} [g_{\alpha\kappa} (1 - \Delta E \hat{\Omega}_\alpha e^{-r_\kappa E_\alpha + f_\kappa})]^{-1}}. \tag{A27}$$

Here $H_{\alpha\kappa}$ is the count of samples with $E \in [E_\alpha, E_\alpha + \Delta E)$ in the time series with $r = r_\kappa$, $g_{\alpha\kappa}$ is a statistical inefficiency factor related to the integrated autocorrelation time of the indicator function for this count, M_κ is the total number of samples for r_κ and $f_\kappa = -\ln Z(r_\kappa)$ is given by

$$f_\kappa = -\ln \sum_\alpha \hat{\Omega}_\alpha \Delta E e^{-r_\kappa E_\alpha}. \tag{A28}$$

Empirically, we find it adequate to set $g_{\alpha\kappa} \equiv 1$. Iteration of Eqs. (A27) and (A28) yields a converged estimate of $\hat{\Omega}_\alpha$ and following Eq. (A26) we compute the estimate of $\langle O \rangle(r)$ as a weighted average of the time series of $\mathcal{O}$ for the different r_κ:

$$\hat{\mathcal{O}}(r) = \frac{\sum_{\kappa=1}^{K} \sum_{n=1}^{M_\kappa} \mathcal{O}_{\kappa n} w_{\kappa n}(r)}{\sum_{\kappa=1}^{K} \sum_{n=1}^{M_\kappa} w_{\kappa n}(r)} \tag{A29}$$

with weights

$$w_{\kappa n}(r) = \sum_\alpha \frac{\psi_{\alpha\kappa n} \hat{\Omega}_\alpha e^{-rE_\alpha}}{\sum_\kappa H_{\alpha\kappa}}, \tag{A30}$$

where $\psi_{\alpha\kappa n}$ is the indicator function for $E \in [E_\alpha, E_\alpha + \Delta E)$ evaluated at the n-th sample of the time series for r_κ.

The multiple histogram reweighting method allows us to finely interpolate between the original values r_κ of our simulations. In addition it provides a reduction of statistical error bars in the reweighted estimates compared to averages from single time series. In this work we have used the method for bosonic observables related to the magnetic transition, although it can easily be extended to all fermionic observables.

Appendix B: Magnetic transition

In the thermodynamic limit the model described by (1) cannot show magnetic long-range order at any $T > 0$ as stated by the Mermin-Wagner theorem [64]. Nevertheless, a finite-temperature phase transition of the Berezinsky-Kosterlitz-Thouless (BKT) type [65–67] is not precluded in this $O(2)$-symmetric model. Defining a local magnetization

$$\vec{m}_i = \frac{1}{\beta} \int_0^\beta \mathrm{d}\tau \vec{\varphi}_i(\tau), \tag{B1}$$

in such a scenario the total magnetization density $\vec{m} = \frac{1}{L^2} \sum_i \vec{m}_i$ vanishes in the thermodynamic limit $L^2 \to \infty$ even below the transition temperature T_{SDW}, where only finite systems will have quasi-long-range order with $\langle |\vec{m}| \rangle \neq 0$. At temperatures approaching T_{SDW} from above the correlation length ξ diverges exponentially

$$\xi \sim \exp\left(b(T - T_{\mathrm{SDW}})^{-\nu}\right), \quad T \to T_{\mathrm{SDW}}^+, \tag{B2}$$

with a critical exponent $\nu = 1/2$ and it stays infinite for all $T \leq T_{\mathrm{SDW}}$, so that the entire low-temperature phase is critical. Spatial correlation functions of the local magnetization fluctuations decay exponentially above T_{SDW} and with a power law below T_{SDW}:

$$\langle \vec{m}_i \cdot \vec{m}_{i+\mathbf{x}} \rangle \sim \begin{cases} e^{-|\mathbf{x}|/\xi}, & T > T_{\mathrm{SDW}}, \\ |\mathbf{x}|^{-\eta(T)}, & T \leq T_{\mathrm{SDW}}. \end{cases} \tag{B3}$$

The critical exponent η depends on temperature with $\eta(T_{\mathrm{SDW}}) = 1/4$. Following e.g. Refs. [68, 69] we study the spin-density wave susceptibility

$$\chi = \beta \sum_i \langle \vec{m}_i \cdot \vec{m}_0 \rangle = \int_0^\beta \mathrm{d}\tau \sum_i \langle \vec{\varphi}_i(\tau) \vec{\varphi}_0(0) \rangle = \beta L^2 \langle \vec{m}^2 \rangle \tag{B4}$$

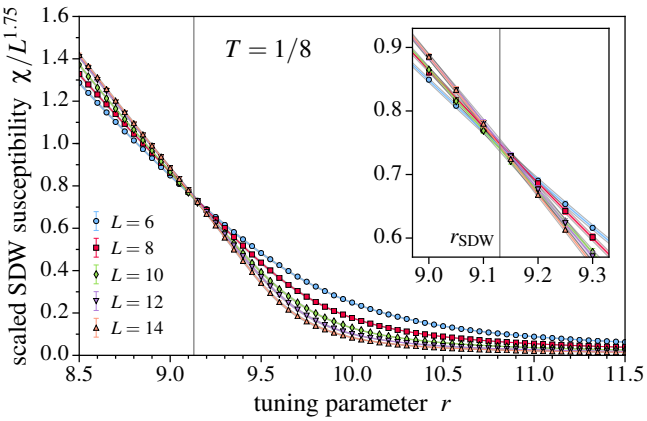

FIG. 8. Scaled SDW susceptibility $\chi/L^{2-\eta_c}$ with $\eta_c = 1/4$ for $T = 1/8$ and various system sizes. Symbols with error bars are estimates from single-r data. Continuous lines with surrounding error regions are results of the multiple-histogram reweighting analysis.

and from Eq. (B3) expect a finite-size scaling behavior like

$$\chi \sim L^{2-\eta} \tag{B5}$$

with $\eta > 0$ for $T \leq T_{\mathrm{SDW}}$ and slightly higher temperatures, where ξ still exceeds L. We identify points (r, T) in the phase diagram where Eq. (B5) can be fitted well to our data with $\eta \leq 1/4$ as belonging to the quasi-long-range ordered SDW phase.

At constant T we scan over r and fit the relation $\ln \chi = \alpha + (2 - \eta) \ln L$ to our data to determine $\eta(r)$. Then we search for $\eta(r_{\mathrm{SDW}}) = 1/4$ to find where $T = T_{\mathrm{SDW}}$. The reweighting technique described in Sec. A 5 provides us with high resolution in r to pinpoint r_{SDW}. In Fig. 8 we show that the intersection point of the scaled SDW susceptibility $\chi/L^{2-\eta_c}$ with $\eta_c = 1/4$ coincides approximately with this estimate for r_{SDW}. Fig. 9 illustrates the dependence of the estimated η on r, while Fig. 10 shows representative examples for fits with $\eta = 1/4$. As it is apparent there, the scaling relation (B5) fits our DQMC well for $T \gtrsim 1/16$, but for $T \leq 1/20$ we cannot find good agreement with the power law on the range of lattice sizes we have accessed. To account for a systematic error at these low temperatures we give a wider estimate of the error on r_{SDW}, allowing for values of $\eta \in [0, 0.5]$ (see Fig. 9b), while at higher temperatures we provide purely statistical error estimates computed from the variance-covariance matrix of the linear fit. A precise quantification of the systematic error in this finite-size scaling analysis would require system sizes L that are larger by orders of magnitude and hence out of computational reach. In Table I we summarize our results for $r_{\mathrm{SDW}}(T)$ as determined from fits over five values $L = 6, \ldots, 14$, which are also plotted in Fig. 1 in the main text, and show in comparison results for a reduced range $L = 8, \ldots, 14$. The data points for $T_{\mathrm{SDW}} \leq 1/20$ in Fig. 1, where we were not able to obtain a good fit, are connected by dotted lines.

The temperature below which the scaling law (B5) may be invalid lies under the superconducting T_c. There we have

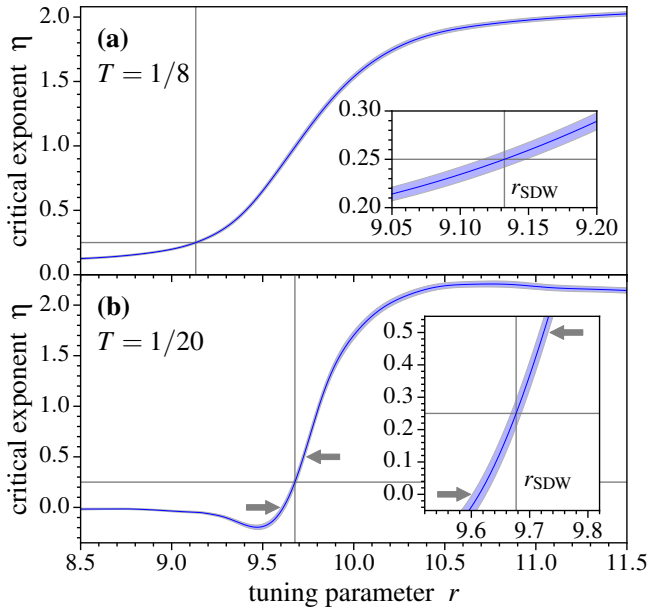

FIG. 9. Critical correlation exponent $\eta(r)$ at (a) $T = 1/8$ and (b) $T = 1/20$ for estimation of $r_{\rm SDW}$, where $\eta = 1/4$. The continuous line shows the result of fitting $\ln\chi = \alpha + (2-\eta)\ln L$ to the DQMC data, which has been interpolated by reweighting. The shaded surrounding region indicates the statistical error. The fits in (b) are of low quality. Here the arrows indicate a wider estimate of the error on $r_{\rm SDW}$, allowing for $\eta \in [0, 0.5]$.

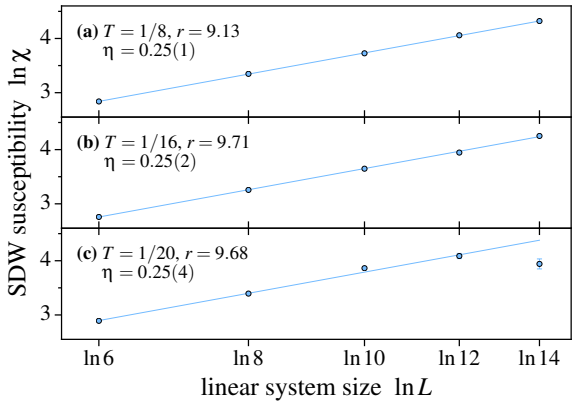

FIG. 10. Best fits of $\ln\chi = \alpha + (2-\eta)\ln L$ with $\eta = 1/4$ for (a) $T = 1/8$, (b) $T = 1/16$, and (c) $T = 1/20$.

some indications that the magnetic transition could be weakly first-order and not of the BKT type. In extensive simulations at $T = 1/20$ for the largest system size $L = 14$ accessed by us the histograms of the finite-system magnetization density show a shallow double-peak structure when we tune r to an intermediate value between the magnetically quasi-long-range ordered and disordered phases, see Fig. 11. The location of this point is marked by a cross in Fig. 1 in the main text. If this dip grows deeper for larger systems, this bimodal distribution can be understood as a sign of phase coexistence at a first-order transition [70]. In our DQMC simulations close

TABLE I. Location of the SDW transition point $r_{\rm SDW}$ for different temperatures T as estimated by fitting $\ln\chi = \alpha + (2-\eta)\ln L$ and searching for $\eta = 1/4$ for two ranges of system sizes $L = 6, \ldots, 14$ ($n = 5$ data points) and $L = 8, \ldots, 14$ ($n = 4$). $\chi^2_{\rm dof} = \chi^2/(n-2)$ is a measure to help with the estimation of the validity of the fit. For $T \le 1/20$ the equation does not fit the data well and $\chi^2_{\rm dof}$ is larger than unity.

	$L = 6, \ldots, 14$		$L = 8, \ldots, 14$	
$1/T$	$r_{\rm SDW}$	$\chi^2_{\rm dof}$	$r_{\rm SDW}$	$\chi^2_{\rm dof}$
4	7.54(3)	0.6	7.6(1)	0.3
5	8.10(3)	1.4	8.07(5)	1.6
6	8.51(4)	1.3	8.499(2)	1.1
8	9.13(2)	0.9	9.12(3)	1.4
10	9.53(1)	0.4	9.52(3)	0.5
12	9.72(1)	1.8	9.73(3)	2.5
13	9.73(1)	0.1	9.73(1)	0.1
14	9.72(1)	4.0	9.76(1)	0.3
16	9.71(1)	0.5	9.71(1)	0.6
20	9.68(8)	10.2	9.7(1)	13.6
26	9.68(5)	11.0	9.66(7)	7.8
30	9.66(6)	4.4	9.62(9)	3.7

to the approximate transition point we also observe noticeably longer statistical autocorrelation times at $T \le 1/20$ than at higher temperatures, which may be explained by the first-order transition and would also make it very cumbersome to obtain sufficient statistics to resolve these histograms for larger L.

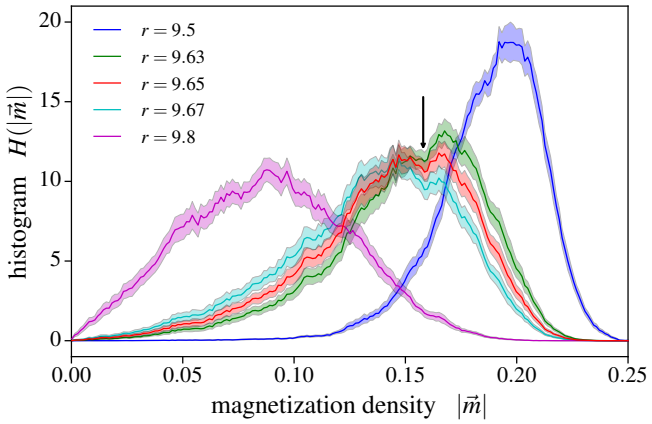

FIG. 11. Low-temperature histograms at $T = 1/20$ and $L = 14$ of the finite-system magnetization density $|\vec{m}|$ show a small suppression between two peaks at $r \approx 9.65$ close to the estimated location of the phase transition. This may be a signature of a weak first-order transition.

Appendix C: Diamagnetic response and the identification of the superconducting T_c

In the appropriate gauge, the linear response of the system to a static, orbital magnetic field $B(\mathbf{q})$ is given by

$$j_x(\mathbf{q}) = -4K_{xx}(\mathbf{q})A_x(\mathbf{q}), \tag{C1}$$

where $A_x(\mathbf{q}) = iB(\mathbf{q})/q_y$ is the vector potential in an appropriate gauge, and

$$K_{xx}(\mathbf{q}) \equiv \frac{1}{4}\left[\Lambda_{xx}(q_x \to 0, q_y = 0) - \Lambda_{xx}(\mathbf{q})\right]. \tag{C2}$$

Here, Λ_{xx} is the current-current correlator

$$\Lambda_{xx}(\mathbf{q}) = \sum_i \int_0^\beta d\tau e^{-i\mathbf{q}\cdot\mathbf{r}_i}\langle j_x(\mathbf{r}_i,\tau)j_x(0,0)\rangle, \tag{C3}$$

and the current density operator is given by $j_x(\mathbf{r}_i) = \sum_{\alpha,s} it_{\alpha i s}\psi^\dagger_{\alpha i s}\psi_{\alpha i s}$ + H.c., where $\mathbf{r}_j = \mathbf{r}_i + \hat{x}$.

In the normal state, the magnetization is given by $-4\mathrm{lim}_{q_y\to 0}K_{xx}/q_y^2$. We note in passing that for general lattice models, the magnetic response can be of either sign. For the band parameters chosen in the text, the response in the non-interacting ($\lambda = 0$) case is paramagnetic.

To identify the superconducting transition, we employ the analysis of Ref. [36]. The superfluid density is given by [37]

$$\rho_s = \lim_{q_y\to 0}\lim_{L\to\infty} K_{xx}(q_x = 0, q_y) \tag{C4}$$

Here, for convenience, we will use the notation $\rho_s(L) = K_{xx}(q_x = 0, q_y = 2\pi/L)$, whose limit when $L \to \infty$ is the superfluid density. At the BKT transition, the superfluid density changes discontinuously by a universal amount, $\Delta\rho_s = \frac{2T}{\pi}$. Figure 12 shows $\rho_s(L)$ across the phase diagram for multiple temperatures. For each temperature we identify the values of r at which $\rho_s(L) > \Delta\rho_s$ as the superconducting phase. The finite-size effects are not very substantial (except perhaps at large r at the lowest temperature $T = 0.025$), and are our main source of error in determining the superconducting phase boundary.

The analysis of the superfluid density does not rely on a particular ansatz for the superconducting order parameter. To determine the symmetry of the superconducting order parameter, we consider the uniform susceptibility $P_\eta(\mathbf{q} = 0)$, as defined in (3). Close to the BKT transition, the susceptibility of the appropriate pairing channel scales as $L^{2-\eta}$, where η varies continuously with temperature, reaching the value $\eta = 0.25$ at T_c.

At low temperatures P_- is strongly dependent on L (see Fig. 2 in the main text). In contrast, P_+ (shown in Fig. 13) remains size-independent. Note also that the s-wave susceptibility is smaller by more than two orders of magnitude than the d–wave one. While we have not attempted to extract the transition temperature from the finite size scaling behaviour of P_-, it is clear that the pairing instability occurs in the d-wave channel.

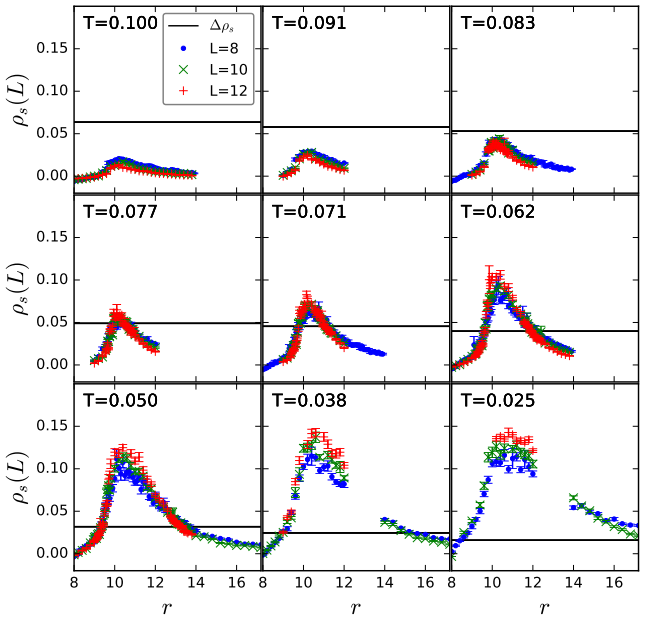

FIG. 12. $\rho_s(L)$, as defined in the text, for system sizes $L = 8, 10, 12$ across the phase diagram. The solid line indicates the universal value $\Delta\rho_s = \frac{2T}{\pi}$ expected at the BKT transition.

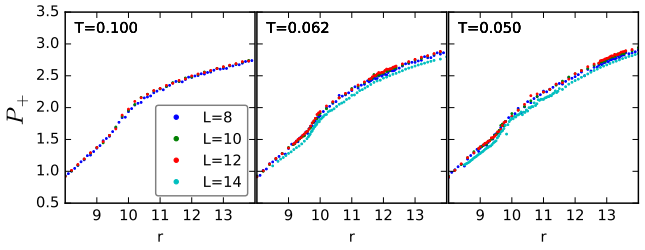

FIG. 13. Superconducting susceptibility in the s–wave channel, P_+, across the phase diagram. Compare to the d–wave susceptibility shown in Fig. 2 in the main text.

Appendix D: Charge and pair density wave

In the main text we have focused on the d-wave CDW and PDW susceptibilities. The s-wave counterparts are shown in Fig. 14. Much like P_-, P_+ shows no structure at finite momenta. C_+ is peaked close to $\mathbf{q} = (\pi, \pi)$ (see also Fig. 15(a)), although the optimal $\mathbf{q}$ can vary slightly with r (not shown). As the temperature is lowered, C_+ is at most moderately enhanced (see Fig. 15(b)), and its maximal value decreases as with decreasing r.

The quasi-one-dimensional character of the fermionic dispersion can account for the enhancement of the CDW susceptibility. In Figure 16 we show the CDW susceptibility for the non-interacting ($\lambda = 0$) case. Note that for this case $C_-(\mathbf{q}) = C_+(\mathbf{q})$. At low temperatures, $C_-(\mathbf{q})$ is peaked at $\mathbf{q} = (\pi, q_{\max}) = (\pi, 0.92\pi)$, similar to the interacting model. As the temperature is lowered, $C_-(\pi, q_{\max})$ increases and saturates at low temperatures, see Fig. 16(b). Compared with C_-

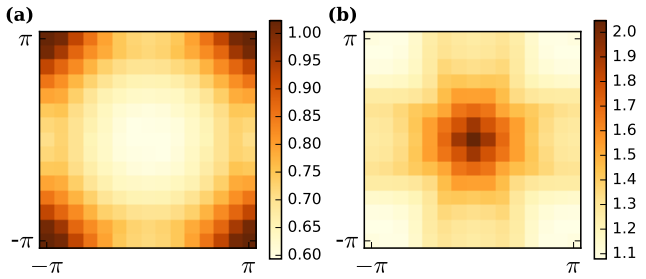

FIG. 14. (a) s-wave CDW and (b) s-wave PDW susceptibilities, as defined in Eq. (3), across the Brillouin zone. Shown here is data for $L = 14$, $T = 0.083$, and $r = 10.4$.

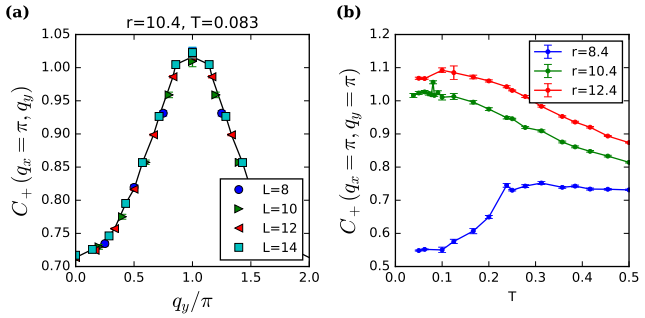

FIG. 15. (a) The s-wave CDW susceptibility versus momentum along the high-symmetry cut $\mathbf{q} = (\pi, q_y)$ for various system sizes. The solid line is a guide to the eye. (b) Temperature dependence of the CDW susceptibility at $q = (\pi, \pi)$ for multiple values of r.

in the interacting case, shown in Fig. 6 of the main text, we see that the maximal CDW susceptibility in the interacting case is about 70% larger than the non-interacting one.

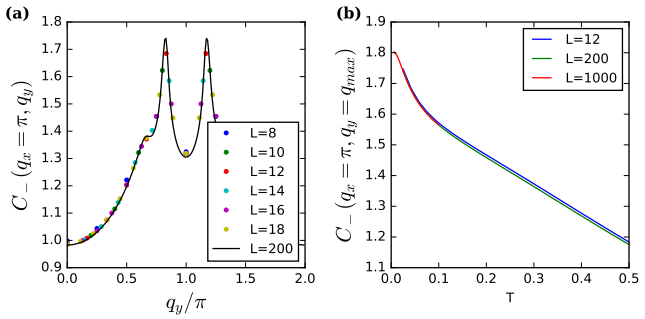

FIG. 16. (a) The non-interacting CDW susceptibility versus momentum along the high-symmetry cut $\mathbf{q} = (\pi, q_y)$ for various system sizes, shown here at $T = 0.025$ (b) Temperature dependence of the non-interacting CDW susceptibility